Observation of a van Hove singularity of a surface Fermi arc with prominent coupling to phonons in a Weyl semimetal

Zhenyu Wang,[1,2,*] Cheng-Yi Huang,[3,*] Chia-Hsiu Hsu,[4,5,9,*] Hiromasa Namiki,[6] Tay-Rong Chang,[7,8,9] Feng-Chuan Chuang,[5,9] Hsin Lin,[3,9] Takao Sasagawa,[6] Vidya Madhavan,[2,†] and Yoshinori Okada[4,‡]

[1]*Department of Physics, University of Science and Technology of China, Hefei, Anhui 230026, China*

[2]*Department of Physics and Frederick Seitz Materials Research Laboratory, University of Illinois Urbana-Champaign, Urbana, Illinois 61801, USA*

[3]*Institute of Physics, Academia Sinica, Taipei, Taiwan*

[4]*Quantum Materials Science Unit, Okinawa Institute of Science and Technology (OIST), Okinawa 904-0495, Japan*

[5]*Department of Physics, National Sun Yat-sen University, Kaohsiung 80424, Taiwan*

[6]*Laboratory for Materials and Structures, Tokyo Institute of Technology, 4259 Nagatsuda, Midori-ku, Yokohama, Kanagawa 226-8503, Japan*

[7]*Department of Physics, National Cheng Kung University, Tainan 701, Taiwan*

[8]*Center for Quantum Frontiers of Research and Technology (QFort), Tainan 701, Taiwan*

[9]*Physics Division, National Center for Theoretical Sciences, Taipei 10617, Taiwan*

(Received 6 May 2021; revised 11 September 2021; accepted 7 January 2022; published 4 February 2022)

A van der Waals coupled Weyl semimetal $NbIrTe_4$ is investigated by combining scanning tunneling microscopy/spectroscopy and first-principles calculations. We observe a sharp peak in the tunneling conductance near the Fermi energy (E_F). Comparison with calculations indicates that the peak originates from a van Hove singularity (vHs) associated with a Lifshitz transition of the surface Fermi-arc state. Interestingly, our tunneling spectroscopy also shows signatures of strong electron-boson coupling. This is potentially due to an anomalously enhanced charge susceptibility coming from the near-E_F vHs formation.

DOI: 10.1103/PhysRevB.105.075110

I. INTRODUCTION

The band structure near the Fermi energy (E_F) governs the physical properties of fermionic systems, and a particularly interesting situation arises when there is a sharp peak in the density of states (DOS) near E_F [1–15]. A large DOS makes the system intrinsically susceptible to Fermi surface instabilities and can be a substantial driving force for emergent phases such as unconventional superconductivity, density wave states, or magnetism, with the added possibility of multiple coexisting phases [15]. Lowering the dimensionality of the system also plays a critical role in accelerating Fermi surface instabilities because the effects of band nesting and electron interactions are inherently enhanced. Furthermore, the enlarged susceptibility can increase electron-boson coupling, which when coupled with Fermi surface instabilities, leads to richly intertwined phenomena involving multiple degree of freedoms [15]. A well-known route to a DOS peak is when a van Hove singularity (vHs), which is typically due to a saddle point in the band dispersion, exists coincidentally near E_F. Such band anomalies near the E_F have been observed and extensively discussed in several material systems, for example, in Cu/Fe-based high-T_c superconductors [7,15], correlated ruthenates [11–14], frustrated lattice systems [8–10], and Dirac materials [5,6]. As exemplified by recent measurements of exotic quantum states in graphene-based systems [5], there is a strong interest in van der Waals (vdW) coupled materials hosting near E_F vHs due to the possibility of using exfoliation and stacking to further tailor the band structure.

An interesting possibility is the realization of vHs and associated many-body effects in topological boundary states [16–20]. For example, prior experiments on topological crystalline insulators have revealed the vHs associated with a Lifshitz transition of the surface state [21]. However, the associated DOS peaks are far from E_F [22–24]. Another promising class of topological materials is Weyl semimetals which feature pairs of doubly degenerate Weyl cones with a linear dispersion around the Weyl nodes in the bulk [25–28]. Weyl semimetals are host to the exotic Fermi arc surface states which eventually morph into bulklike states, that is, they sink into a pair of Weyl points with opposite charge chirality. Recent studies on the band structure of Weyl semimetals have suggested a possible topological Lifshitz transition near the Weyl points with an interesting surface Fermi arc that rewires at different energies [29–31]. However, a singularity with a peak in the DOS near the E_F and associated many-body effect have not been reported experimentally.

In this study, we combine scanning tunneling microscopy/spectroscopy (STM/S) and first-principles calculations to investigate a vdW coupled Weyl semimetal $NbIrTe_4$. This ternary compound is known as a type-II Weyl semimetal with relatively simple topological Fermi-arc states with fewer Weyl points than those of $MoTe_2$ [32–36]. Our present study shows a near-E_F topologically nontrivial Fermi-arc derived vHs with prominent coupling to phonons.

*These authors contributed equally to this work.
†vm1@illinois.edu
‡yoshinori.okada@oist.jp

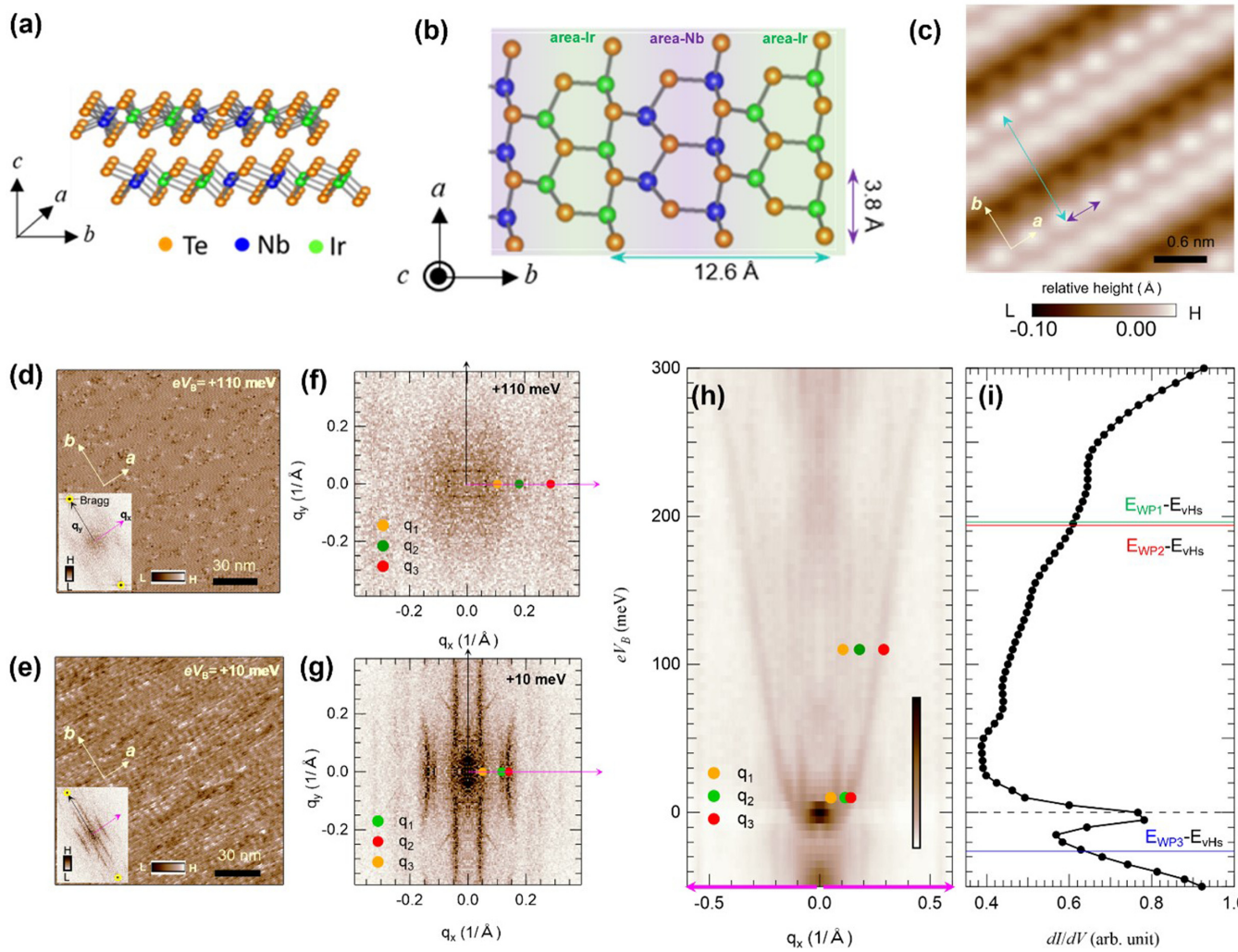

FIG. 1. Characteristics of the Weyl semimetal $NbIrTe_4$. (a), (b) Schematic of the crystal structure of $NbIrTe_4$ with side and top views, respectively. (c) STM topographic image with atomic resolution ($I_t = 100$ pA and $V_B = 100$ mV). The scale of arrows corresponds to that in (b). (d), (e) Conductance (dI/dV) maps at $eV_B = 110$ and 10 meV, respectively. The insets show the raw FT of the dI/dV images, where Bragg peaks are highlighted by circles. (f), (g) The rotated and twofold symmetrized FT images of that in the inset of (d), (e). Here, the horizontal and vertical axes are set along the crystal axes a and b, respectively. (h) Intensity plot of the line cut in the FTs along the q_x direction at $q_y = 0$, together with scattering vectors $q_1 \sim q_3$ in (f) and (g). (i) The spatially averaged dI/dV spectrum, which is taken simultaneously with QPI imaging. Theoretical three energies for WP, to be compared with experiment, are indicated by horizontal lines (see main body for details). The FT images in (d)–(g) and (h), (i) are from different measurement settings. (d)–(g) were set for aiming to get high-quality q with better resolution and signal to noise ratio, whereas (h) and (i) were to collect overall dispersion for wider energy region. Note that data were taken from the same area.

II. METHODS

Single crystals of $NbIrTe_4$ were grown by a Te-flux method. The samples were characterized by x-ray diffraction and x-ray fluorescence to confirm single-phase growth without phase segregation. Samples were cleaved in ultrahigh vacuum at ~80 K and then immediately inserted into the cold STM head. All the data were obtained at 300 mK in zero external magnetic field. Tungsten STM tips were checked on a Cu(111) surface prior to use. The differential conductance (dI/dV), which is proportional to DOS, was measured using standard lock-in technique, with the frequency of the bias modulation set to 987.5 Hz. Density-functional theory (DFT) band calculations were performed using the projector augmented-wave method as implemented in the VASP package [37] within the generalized gradient approximation [38]. In all calculations, spin-orbit coupling was included self-consistently.

III. RESULTS AND DISCUSSION

A. Sharp quasiparticle interference and conductance (dI/dV) peak near zero bias voltage

The crystal structure of $NbIrTe_4$ is shown in Figs. 1(a) and 1(b). $NbIrTe_4$ is expected to be in the $1T$ phase and the surface termination is expected to be the (001) plane which is the vdW coupled Te atomic sheet. From the zoomed topographic image [Fig. 1(c)], we find atomic periodicity of 3.8 Å along a (purple

arrow) and 12.6 Å along b (blue arrow) which are consistent with the expected crystal structure of $NbIrTe_4$ [see Fig. 1(b)].

Our STM studies on $NbIrTe_4$ reveal the existence of sharp quasiparticle interference (QPI) patterns and dI/dV peak near E_F (E_F corresponds to the bias voltage $V_B = 0$). QPI measurements have been widely used to investigate the dispersion of topological surface states in Weyl semimetals [39–45]. In $NbIrTe_4$, while the dI/dV map at $eV_B = 110$ meV shows faint real-space scattering patterns confined sharply to the scattering centers [Fig. 1(d)], the dI/dV map at $eV_B = 10$ meV shows apparent wavelike patterns that can be tracked over several wavelengths [Fig. 1(e)]. This difference is better visualized by a Fourier transformation (FT) of the dI/dV maps. Shown in Figs. 1(d) and 1(e) and Figs. 1(f) and 1(g) are the dI/dV maps and their twofold symmetrized counterparts at two different energies. Sharp patterns with well-defined scattering channels labeled $q_1 \sim q_3$ are seen at $eV_B = 10$ meV [Fig. 1(g)]. The QPI dispersion along q_x, obtained from a series of maps at different energies, is shown in Fig. 1(h). We find that the magnitude of the q vector for all three scattering channels goes to zero near E_F, which suggests the existence of constant energy contours potentially touching each other, thereby hosting a saddle point near E_F. Interestingly, a corresponding sharp peak is observed in the dI/dV spectra at the same energy [Fig. 1(i)]. This sharp dI/dV peak was observed everywhere on the surface (Supplemental Material note 1, SM1 [46]) and is therefore intrinsic characteristic of $NbIrTe_4$ and not due to a disorder-generated local state. The peak position differs within an ∼10-meV scale as we go from area to area separated by long distances (micrometers) as shown in SM2 [46].

To understand the origin of this near-E_F electronic anomaly, we carry out DFT calculations (details in SM3 [46]). Figure 2(a) shows the Brillouin zones (BZ) of the bulk (lower) and surface (upper), and Fig. 2(b) shows the three pairs of irreducible Weyl points (WP1, WP2, and WP3), depicted by color-coded circles and squares along with their energies E_{WP1}, E_{WP2}, and E_{WP3} (136, 134, and −86 meV), respectively. Since the spectral weight of the topologically nontrivial Fermi-arc surface state (NSS) must sink into the bulk states through Weyl points, the NSS can be qualitatively disentangled from trivial surface state (TSS) by looking for this characteristic spectral fingerprint.

Figures 2(c) and 2(d) show the total-surface spectral-weight maps at 134 and −50 meV, respectively. As shown in Fig. 2(e), which is the momentum region highlighted by the pink rectangle in Fig. 2(c), spectral weight [indicated by arrow (NSS2)] sinks into the bulk bands through WP2. Similarly, tracking the spectral weight as it sinks into WP3 enables us to identify another Fermi arc. Figure 2(f) shows dispersion along the vertical line with an arrow in Fig. 2(d), and spectral feature indicated by arrow (NSS3) sinks into the bulk bands through WP3. Here, the spectral-weight sinking behavior into WP2 and WP3 in the momentum space is highlighted by the dashed lines in Figs. 2(e) and 2(f), respectively. An interesting feature from the band calculation is the dominant contribution of the Nb states in the NSS (see also SM4 for details [46]). Figure 2(h) shows the atomic character of the dispersion shown in Fig. 2(g). The dominant contribution of Nb for NSS2 and NSS3 is clearly visualized (see arrows).

Before proceeding further, we briefly discuss the unusual connection of NSS2 and NSS3 in momentum space.

Figure 2(g) shows energy evolution of total surface spectral weight (NSS and TSS) along k_x at fixed $k_y = \pi/b$ [see horizontal arrows in Fig. 2(e)]. Around the momentum highlighted by dashed circle [see Fig. 2(g)], NSS2 and NSS3 merge with each other. This means that NSS2 and NSS3 host a single Fermi arc state, which connect two pairs of Weyl points instead of the conventional case where only one pair of Weyl points is connected. We believe that this band touching is accidental and is not forbidden since the number of nontrivial surface states emerging from a paired Weyl nodes remains the same number, one.

IV. FERMI-ARC vHS AND ASSOCIATED LIFSHITZ TRANSITION

In the pristine DFT calculation, NSS3 hosts a Lifshitz transition at a characteristic energy E_{vHs}, whose value in the calculation is around −60 meV. This can be clearly seen by focusing on the momentum region highlighted by the rectangle in Fig. 2(d) as shown in Figs. 3(a)–3(e). From the figure, we see that the constant energy contours of the Fermi arcs near the E_{vHs} show geometrical changes across E_{vHs}. This can be seen more clearly in the comparison between the three-dimensional plot of NSS dispersion (upper panel) and $1/|\nabla_k E|$ map (lower panel) in Fig. 3(f). As the total DOS is proportional to $\int 1/|\nabla_k E(k)|dk$, the $1/|\nabla_k E|$ map provides an excellent way to visualize the characteristic momentum leading to an enhanced DOS. The plot demonstrates that the momentum position leading to large DOS corresponds to momentum hosting the Lifshitz transition. We note that this Lifshitz transition arises from the single-band NSS3. To show this, the line cut along $k_y = 0.182$ Å^{-1} [Fig. 3(a)], which is slightly off from momentum of vHs, is shown in Fig. 3(g). The saddle point seen along the k_y direction, which results in electronlike band curvature, is indicated by dashed circle in Fig. 3(g). As seen, single NSS3 is forming vHs while NSS2 is away from corresponding momentum. The associated vHs shows up as a peak in the calculated DOS of the NSS [Fig. 3(h)]. The natural question then is whether the peak near the Fermi energy seen in the experimental data arises from this Lifshitz transition. As we show in the next section, comparison of the QPI-derived dispersion as well as the constant energy contour demonstrates that this is indeed the case.

V. COMPARISON BETWEEN EXPERIMENT AND THEORY

To compare the data with the calculation, we plot the experimentally obtained dispersion and the theoretical dispersion using E_{vHs} as a reference. This would correspond to a situation where the experimental DOS peak near E_F originates from vHs associated with the Lifshitz transition seen in the theory and would imply that the calculated band structure must be shifted by 60 meV to match the experiments. We find good agreement between the experimentally derived dispersion from QPI [Fig. 4(a)] and calculated joint DOS (JDOS)-derived dispersion [Fig. 4(b)] along the q_x direction. Furthermore, the experimental QPI and theoretical JDOS

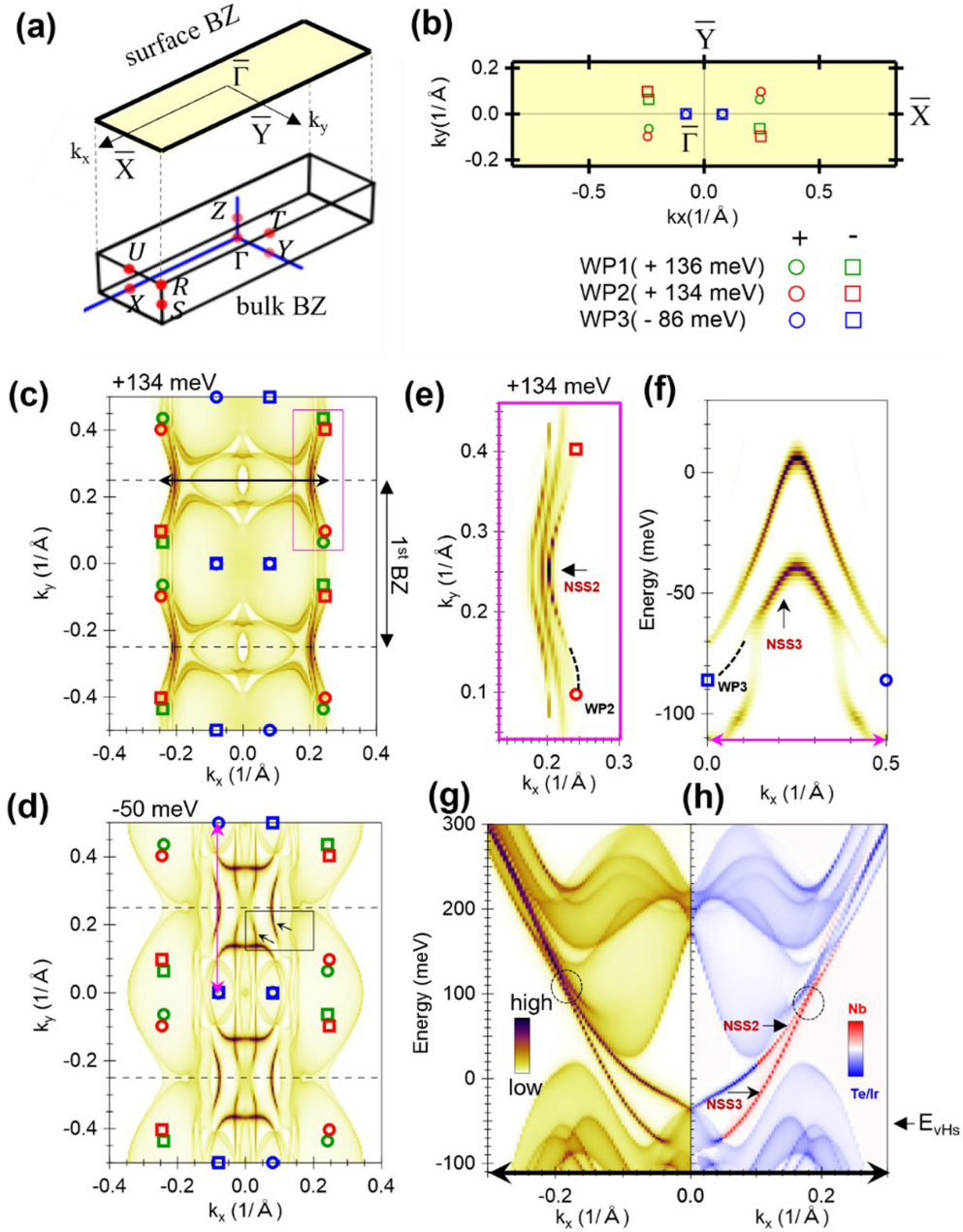

FIG. 2. The DFT calculation for electronic state of NbIrTe4. (a) BZ of the system. (b) The calculated WPs with their momentum, energy, and chirality. (c), (d) Total spectral weight on the surface plotted at 134 meV, the energy of WP2, and at −50 meV near the energy of the vHS. The total surface spectral weight contains TSS and NSS contributions. The Weyl points WP1 (green), WP2 (red), and WP3 (blue) are indicated in the momentum space. (e) Zoomed-in image of the pink rectangle in (c), and (f) dispersion along the pink line in (d). The dashed lines in (e) and (f) indicate the trace along which the NSSs sink into the bulk state through Weyl points. (g) Energy dispersion along the k_x direction at $k_y = \pi/b$ [see horizontal line in (c)] for total spectral weight and (h) its atomic character dependence. The dashed circle indicates the energy where NSS2 and NSS3 merge (see main body for details). Note that the band merging indicated by dashed circle (∼+100 meV) is different from van Hove singularity at $E_{v\mathrm{Hs}}$ [see right axis of (h)].

plotted in q_x-q_y space at a fixed energy, also agree well [Fig. 4(d)]. (The small quantitative mismatch between experimental scattering vectors and theoretical JDOS will be explained in the next section.) This allows us to conclude that the experimental *dI/dV* peak near E_F originates from vHs associated with the Lifshitz transition of the NSS.

The comparison also allows us to identify the origins of the q vectors seen in the experimental QPI (see SM5). The theoretical spectral-weight distribution in the k_x-k_y plane for $E - E_{v\mathrm{Hs}} = 10\,\mathrm{meV}$, as well as the scattering vector candidates (q_{tss}, q_{i}, q_{ii}, and q_{iii}), are shown in Fig. 4(c). By comparing QPI patterns at $eV_B = 10\,\mathrm{meV}$ [Fig. 4(d), upper] and NSS-derived JDOS at $E - E_{v\mathrm{Hs}} = 10\,\mathrm{meV}$ [Fig. 4(d), lower], the experimental q_1, q_2, q_3, and their extension in $q_x - q_y$ space are beautifully explained as intra-NSS scattering channel q_{i}, q_{ii}, and q_{iii}, respectively. Since the JDOS calculation captures the QPI well, we expect that the spin-based matrix elements must be nonzero for all the q vectors q_{i}, q_{ii}, and q_{iii}.

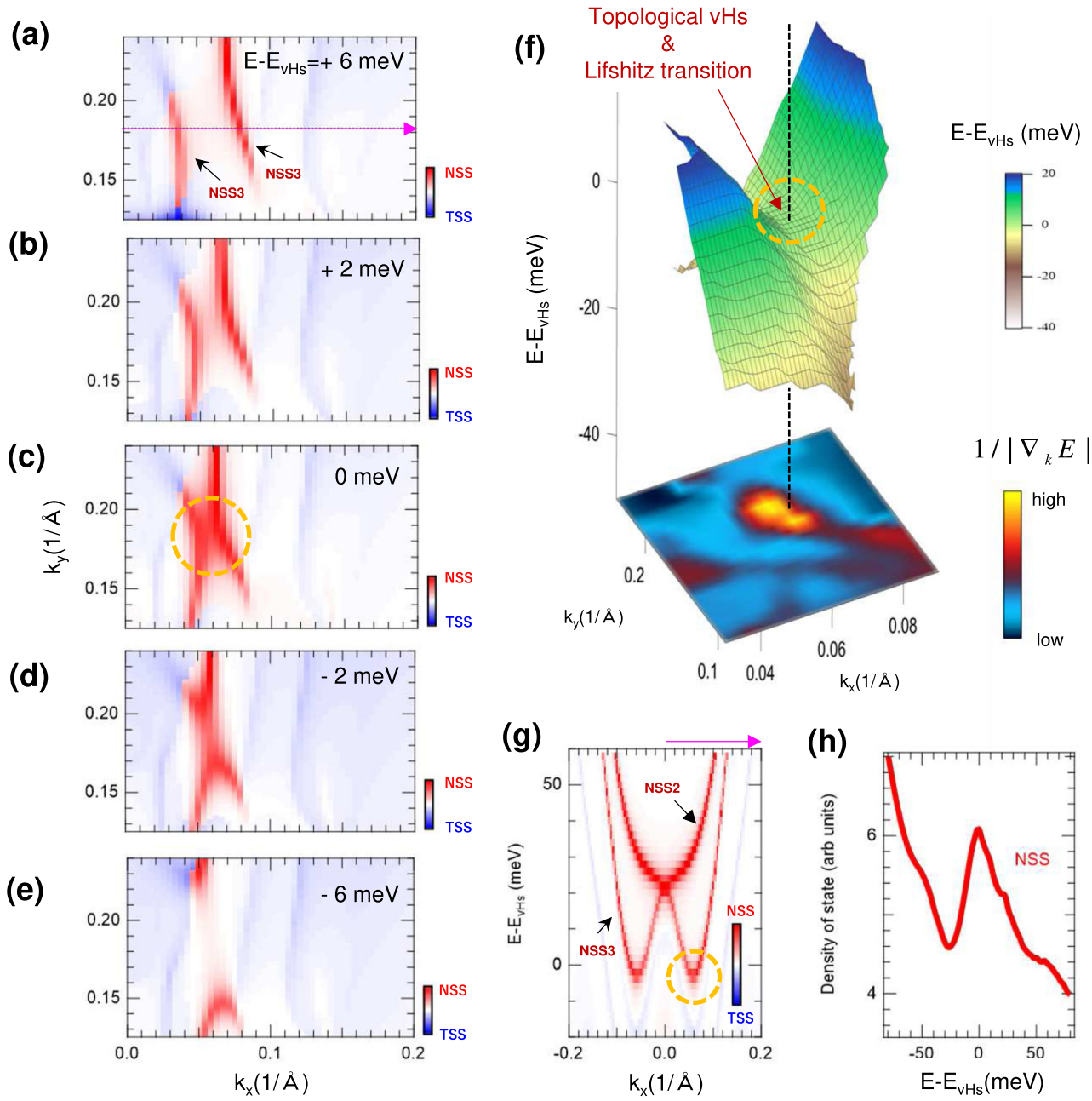

FIG. 3. Electronic structure calculation near the energy for van Hove singularity $E_{\rm vhs}$. (a)–(e) Energy evolution of spectral weight for the area indicated by the dashed rectangle in Fig. 2(d). (f) Three-dimensional display of NSS dispersion (upper part) and $1/|\nabla_k E|$(lower part), near the critical momentum as in (c). (g) The energy dispersion along the horizontal arrow in (a). The vHs formations associated with a Lifshitz transition are indicated by an arrow and dashed circle in (c), (f), and (g). (h) Calculated DOS for NSS, which is obtained by integrating the spectral weight over all the momenta in the first BZ.

This was confirmed by calculating the spin-resolved spectral weight for NSS at $E - E_{\rm F} = 10\,$meV (see main SM6 for details [46]).

VI. SPECTROSCOPIC SIGNATURE OF ELECTRON-BOSON COUPLING

Interestingly, a closer look at the *dI/dV* spectra at energies around E_F reveals a prominent signature of electron-boson coupling. Figure 5(a) shows a topographic image in which 2116 tunneling spectra were acquired near the E_F. The averaged *dI/dV* and d^2I/dV^2 spectra are shown in Figs. 5(b) and 5(c), respectively. Dip and hump features, which are symmetric with respect to the E_F, are observed in the *dI/dV*. The clear peaks in d^2I/dV^2 indicate a strong coupling of electrons to a bosonic mode. Here, we define E_p as the DOS peak energy corresponding to the vHs, and E^+ and E^- as the peak positions in d^2I/dV^2 corresponding to coupling with the phonon mode. We note that this strong electron-boson coupling also explains the small quantitative mismatch between experimental

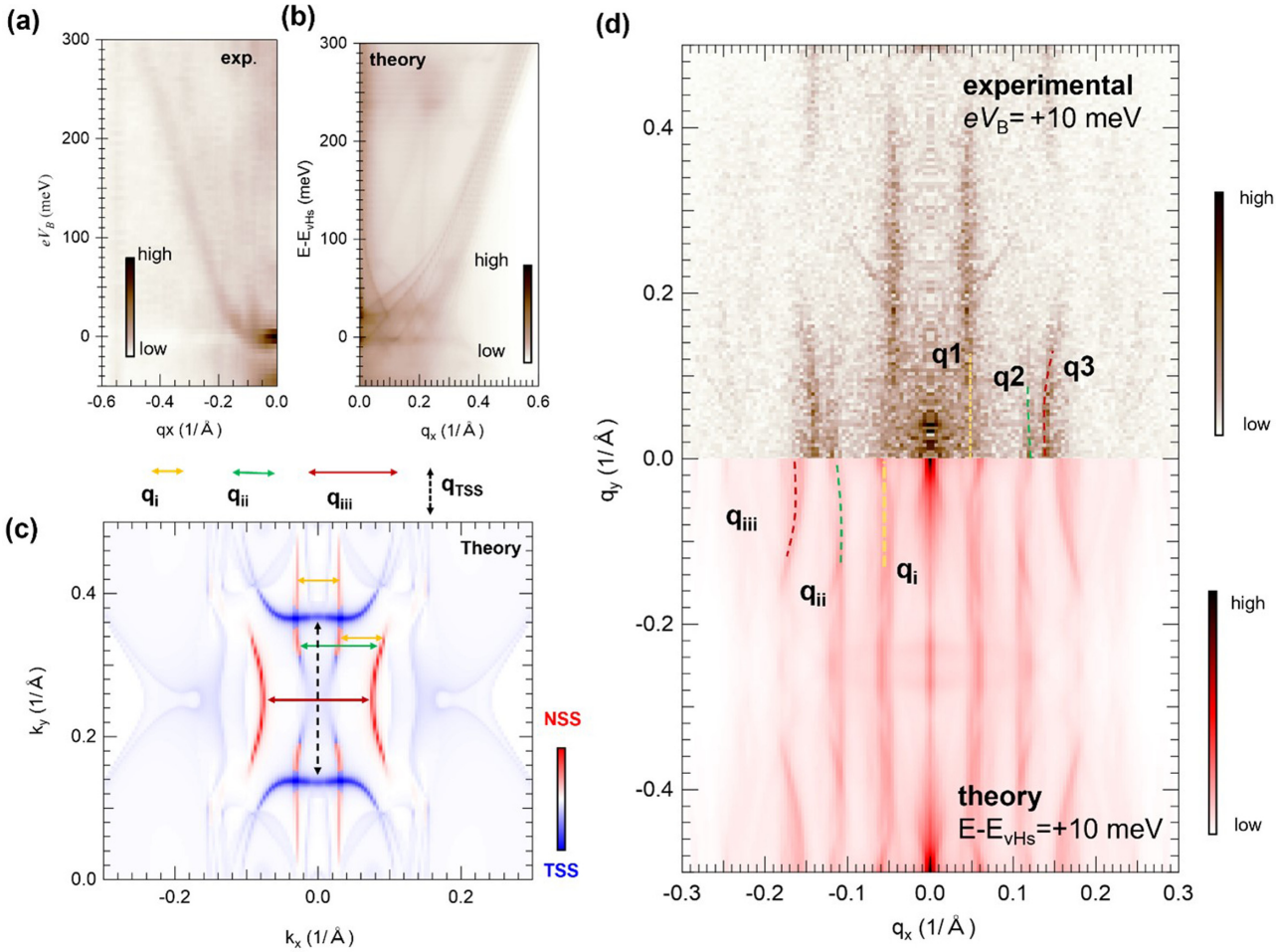

FIG. 4. The comparison between theory and experiments. (a), (b) The experimental energy evolution of QPI pattern and the theoretical JDOS of the total spectral weight along q_x direction at $q_y = 0$. Here, vertical axis in (b) is plotted energy relative to vHs. (c) Calculated spectral weight in *kx-ky* space at $E - E_{vHs} = 10$ meV. Here, the rectangle is the momentum area focused in Fig. 3 to represent vHs and associated Lifshitz transition. (d) Comparison between the experimental QPI (upper) and theoretical JDOS sorely from NSS (lower) at $eV_B = 10$ meV and $E - E_{vhs} = 10$ meV, respectively.

scattering vectors and the theoretical JDOS, which was obtained without considering interaction effects [Fig. 4(d)].

Since the dominant contribution to the vHs is from Nb derived bands, we can expect to see spatial modulations of the intensity of the DOS peak and bosonic-mode coupling. This is confirmed by a comparison between topographic height [Fig. 5(d)], *dI/dV* [Fig. 5(e)], and d^2I/dV^2 [Fig. 5(f)] across the line A-B in Fig. 5(a). We find that the spatial modulation of experimental vHs peak intensity near E_F [Fig. 5(e)] shows good agreement with periodic modulation of topographic image [Fig. 5(d)]. Since vHs is dominated by Nb-derived spectral weight, we speculate that the location with large vHs peak intensity is close to Nb [indicated by "area Nb" in Figs. 1(b), Fig. 5(d) and 5(f)]. We also note that E^+ and E^- appear almost symmetrically relative to the E_F at every location, which further supports our identification of E^+ and E^- as inelastic modes. As our system is not magnetic, the bosonic mode is more likely to be a phonon. Indeed, the experimental energy scale of $|E^+|$ and $|E^-|$ ($\sim$35 meV) is comparable to an optical phonon in the calculation at 32 meV. We note that this current comparison is with bulk phonons (SM7 for details [46]), and we leave a direct comparison with surface phonons for future study. An interesting finding in our data is that the $|E^+|$ and $|E^-|$ values are larger in the area Nb, compared to "area Ir" [Fig. 1(b) and Fig. 5(f)]. This may be due to the fact that the different phonon modes may be mixed in with different weights at the various lattice positions (see SM8 for details [46]). The prominent electron-phonon coupling seen in our data represents an enhanced charge susceptibility due to vHs formation near E_F. These findings provide an interesting route to modulate topologically nontrivial vHs via phonon engineering [47–50]. Similarly, coupling to an acoustic plasmon mode as reported recently in Bi_2Te_3 [51] may also enrich many-body effects near E_F.

VII. SUMMARY

In summary, we report observation of near-E_F Fermi-arc vHs with prominent coupling to phonons in a vdW coupled Weyl semimetal $NbIrTe_4$. Such near-E_F vHs in vdW coupled Weyl semimetal is particularly interesting due to the possibility of using exfoliation, stacking, gating, and strain to further tune the electronic properties and search for exotic topological and correlated phases.

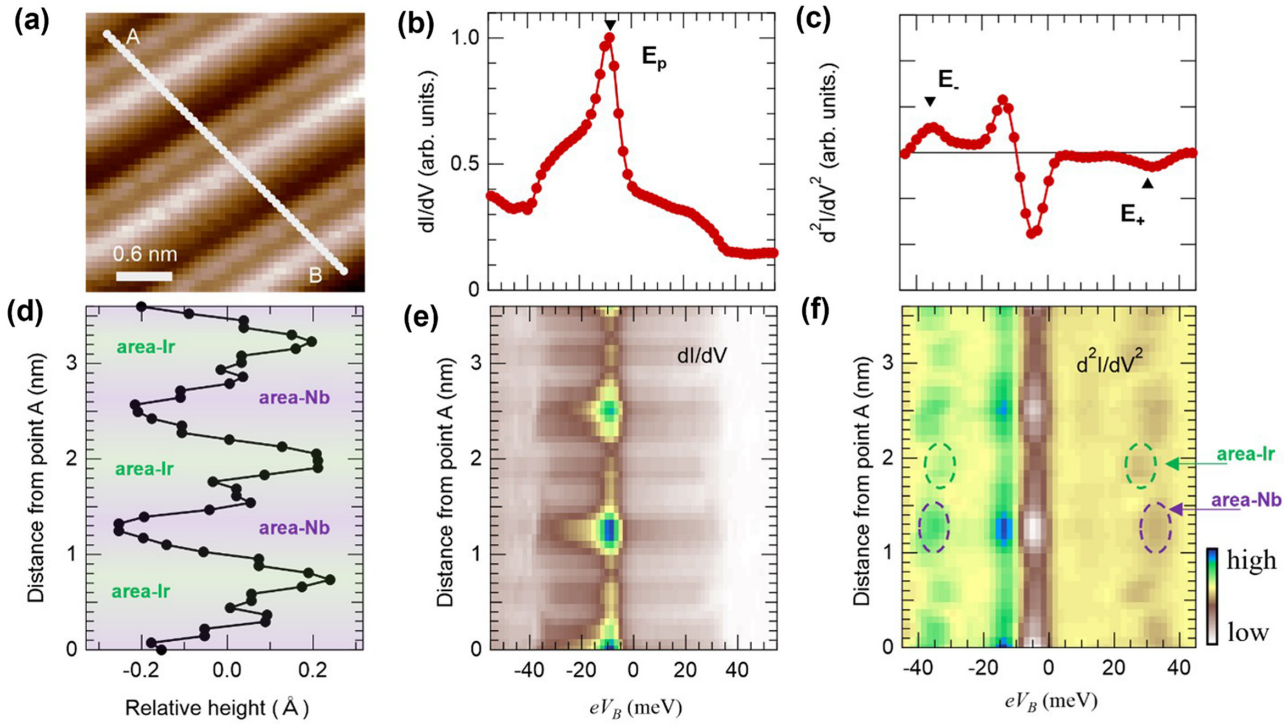

FIG. 5. Enhanced electron-mode coupling. (a) Topographic image ($I_t = 100$ pA and $V_B = 100$ mV). (b), (c) Spatial average of dI/dV and d^2I/dV^2 spectra. The spectra are averaged from 2116 curves (46 × 46 pixels) from the area shown in (a). (d) Topographic height variations along A-B in (a). (e), (f) Spatial evolution of dI/dV and d^2I/dV^2 spectra taken along A-B shown in (a).

ACKNOWLEDGMENTS

Work at the University of Illinois, Urbana-Champaign was supported by U.S. Department of Energy (DOE), Office of Science, Office of Basic Energy Sciences (BES), Materials Sciences and Engineering Division under Award No. DE-SC0022101. Z.Y.W. is supported by National Natural Science Foundation of China (Grant No. 12074364) and the Fundamental Research Funds for the Central Universities (Grant No. WK3510000012). This work was, in part, supported by JST-CREST Project No. JPMJCR16F2 and a JSPS Grants-in-Aid for Scientific Research (A) Grant No. 21H04652. F.C.C. acknowledges support from the National Center for Theoretical Sciences and the Ministry of Science and Technology of Taiwan under Grant No. MOST-110-2112-M-110-013-MY3. F.C.C. is also grateful to the National Center for High-performance Computing for computer time and facilities. H.L. acknowledges the support by the Ministry of Science and Technology (MOST) in Taiwan under Grant No. MOST 109-2112-M-001-014-MY3. T.-R.C. was supported by the Young Scholar Fellowship Program under a MOST grant for the Columbus Program, MOST110-2636-M-006-016, the Higher Education Sprout Project, Ministry of Education to the Headquarters of University Advancement at the National Cheng Kung University (NCKU), the National Center for Theoretical Sciences (Taiwan).

[1] L. Van Hove, The occurrence of singularities in the elastic frequency distribution of a crystal, Phys. Rev. **89**, 1189 (1953).

[2] V. Madhavan, W. Chen, T. Jamneala, M. F. Crommie, and N. S. Wingreen, Tunneling into a single magnetic atom: Spectroscopic evidence of the Kondo resonance, Science **280**, 567 (1998).

[3] A. R. Schmidt, M. H. Hamidian, P. Wahl, F. Meier, A. V. Balatsky, J. D. Garrett, T. J. Williams, G. M. Luke, and J. C. Davis, Imaging the Fano lattice to 'hidden order' transition in URu_2Si_2, Nature (London) **465**, 570 (2010).

[4] P. Aynajian, E. H. S. Neto, A. Gyenis, R. E. Baumbach, J. D. Thompson, Z. Fisk, E. D. Bauer, and A. Yazdani, Visualizing heavy fermions emerging in a quantum critical Kondo lattice, Nature (London) **486**, 201 (2012).

[5] G. Li, A. Luican, J. M. B. Lopes dos Santos, A. H. Castro Neto, A. Reina, J. Kong, and Y. E. Andrei, Observation of Van Hove singularities in twisted graphene layers, Nat. Phys. **6**, 109 (2010).

[6] D. V. Chichinadze, L. Classen, and A. V. Chubukov, Valley magnetism, nematicity, and density wave orders in twisted bilayer graphene, Phys. Rev. B **102**, 125120 (2020).

[7] X. Shi, Z.-Q. Han, X.-L. Peng, P. Richard, T. Qian, X.-X. Wu, M.-W. Qiu, S. C. Wang, J. P. Hu, Y.-J. Sun, and H. Ding, Enhanced superconductivity accompanying a Lifshitz transition in electron-doped FeSe monolayer, Nat. Commun. **8**, 14988 (2017).

[8] S. S. Zhang, J.-X. Yin, M. Ikhlas, H.-J. Tien, R. Wang, N. Shumiya, G. Chang, S. S. Tsirkin, Y. Shi, C. Yi, Z. Guguchia,

H. Li, W. Wang, T.-R. Chang, Z. Wang, Y.-f. Yang, T. Neupert, S. Nakatsuji, and M. Z. Hasan, Many-Body Resonance in a Correlated Topological Kagome Antiferromagnet, Phys. Rev. Lett. **125**, 046401 (2020).

[9] Z. Lin, J.-H. Choi, Q. Zhang, W. Qin, S. Yi, P. Wang, L. Li, Y. Wang, H. Zhang, Z. Sun, L. Wei, S. Zhang, T. Guo, Q. Lu, J.-H. Cho, C. Zeng, and Z. Zhang, Flat Bands and Emergent Ferromagnetic Ordering in Fe_3Sn_2 Kagome Lattices, Phys. Rev. Lett. **121**, 096401 (2018).

[10] J.-X. Yin, N. Shumiya, S. Mardanya, Q. Wang, S. S. Zhang, H.-J. Tien, D. Multer, Y. Jiang, G. Cheng, N. Yao, S. Wu, D. Wu, L. Deng, Z. Ye, R. He, G. Chang, Z. Liu, K. Jiang, Z. Wang, T. Neupert, A. Agarwal, T.-R. Chang, C.-W. Chu, H. Lei, and M. Z. Hasan, Fermion–boson many-body interplay in a frustrated kagome paramagnet, Nat. Commun. **11**, 4003 (2020).

[11] K. Iwaya, S. Satow, T. Hanaguri, N. Shannon, Y. Yoshida, S. I. Ikeda, J. P. He, Y. Kaneko, Y. Tokura, T. Yamada, and H. Takagi, Local Tunneling Spectroscopy across a Metamagnetic Critical Point in the Bilayer Ruthenate Sr_3Ru_2O, Phys. Rev. Lett. **99**, 057208 (2007).

[12] Z. Wang, D. Walkup, P. Derry, T. Scaffidi, M. Rak, S. Vig, A. Kogar, I. Zeljkovic, A. Husain, L. H. Santos, Y. Wang, A. Damascelli, Y. Maeno, P. Abbamonte, E. Fradkin, and V. Madhavan, Quasiparticle interference and strong electron–mode coupling in the quasi-one-dimensional bands of Sr_2RuO_4, Nat. Phys. **13**, 799 (2017).

[13] C. A. Marques, L. C. Rhodes, R. Fittipaldi, V. Granata, C. M. Yim, R. Buzio, A. Gerbi, A. Vecchione, A. W. Rost, and P. Wahl, The surface layer of Sr_2RuO_4: A two-dimensional model system for magnetic-field-tuned quantum criticality, arXiv:2005.00071.

[14] B. Burganov, C. Adamo, A. Mulder, M. Uchida, P. D. C. King, J. W. Harter, D. E. Shai, A. S. Gibbs, A. P. Mackenzie, R. Uecker, M. Bruetzam, M. R. Beasley, C. J. Fennie, D. G. Schlom, and K. M. Shen, Strain Control of Fermiology and Many-Body Interactions in Two-Dimensional Ruthenates, Phys. Rev. Lett. **116**, 197003 (2016).

[15] R. S. Markiewicz, A survey of the Van Hove scenario for high-Tc superconductivity with special emphasis on pseudo-gaps and striped phases, J. Phys. Chem. Solids **58**, 1179 (1997).

[16] Z.-H. Pan, A. V. Fedorov, D. Gardner, Y. S. Lee, S. Chu, and T. Valla, Measurement of an Exceptionally Weak Electron-Phonon Coupling on the Surface of the Topological Insulator Bi_2Se_3 Using Angle-Resolved Photoemission Spectroscopy, Phys. Rev. Lett. **108**, 187001 (2012).

[17] X. Zhu, L. Santos, C. Howard, R. Sankar, F. C. Chou, C. Chamon, and M. El-Batanouny, Electron-Phonon Coupling on the Surface of the Topological Insulator Bi_2Se_3 Determined from Surface-Phonon Dispersion Measurements, Phys. Rev. Lett. **108**, 185501 (2012).

[18] T. Kondo, Y. Nakashima, Y. Ota, Y. Ishida, W. Malaeb, K. Okazaki, S. Shin, M. Kriener, S. Sasaki, K. Segawa, and Y. Ando, Anomalous Dressing of Dirac Fermions in the Topological Surface State of Bi_2Se_3, Bi_2Te_3, and Cu-Doped Bi_2Se_3, Phys. Rev. Lett. **110**, 217601 (2013).

[19] X. Zhu, C. Howard, J. Guo, and M. El-Batanouny, Electron-Phonon Coupling on the Surface of Topological Insulators, arXiv:1307.4559.

[20] G. B. Osterhoudt, Y. Wang, C. A. C. Garcia, V. M. Plisson, J. Gooth, C. Felser, P. Narang, and K. S. Burch, Evidence for Dominant Phonon-Electron Scattering in Weyl Semimetal WP_2, Phys. Rev. X **11**, 011017 (2021).

[21] T. H. Hsieh, H. Lin, J. Liu, W. Duan, A. Bansil, and L. Fu, Topological crystalline insulators in the SnTe material class, Nat. Commun. **3**, 982 (2012).

[22] Y. Okada, M. Serbyn, H. Lin, D. Walkup, W. Zhou, C. Dhital, M. Neupane, S. Xu, Y. J. Wang, R. Sankar, F. Chou, A. Bansil, M. Z. Hasan, S. D. Wilson, L. Fu, and V. Madhavan, Observation of Dirac node formation and mass acquisition in a topological crystalline insulator, Science **341**, 1496 (2013).

[23] I. Zeljkovic, Y. Okada, M. Serbyn, R. Sankar, D. Walkup, W. Zhou, J. Liu, G. Chang, Y. J. Wang, M. Z. Hasan, F. Chou, H. Lin, A. Bansil, L. Fu, and V. Madhavan, Dirac mass generation from crystal symmetry breaking on the surfaces of topological crystalline insulators, Nat. Mater. **14**, 318 (2015).

[24] I. Zeljkovic, K. L. Scipioni, D. Walkup, Y. Okada, W. Zhou, R. Sankar, G. Chang, Y. J. Wang, H. Lin, A. Bansil, F. C. Chou, Z. Wang, and V. Madhavan, Nanoscale determination of the mass enhancement factor in the lightly doped bulk insulator lead selenide, Nat. Commun. **6**, 6559 (2015).

[25] S. Murakami, Phase transition between the quantum spin Hall and insulator phases in 3D: Emergence of a topological gapless phase, New J. Phys. **9**, 356 (2007).

[26] X. Wan, A. M. Turner, A. Vishwanath, and S. Y. Savrasov, Topological semimetal and Fermi-arc surface states in the electronic structure of pyrochlore iridates, Phys. Rev. B **83**, 205101 (2011).

[27] A. A. Burkov and Leon Balents, Weyl Semimetal in a Topological Insulator Multilayer, Phys. Rev. Lett. **107**, 127205 (2011).

[28] G. Xu, H. Weng, Z. Wang, X. Dai, and Z. Fang, Chern Semimetal and the Quantized Anomalous Hall Effect in HgCr2Se4, Phys. Rev. Lett. **107**, 186806 (2011).

[29] G. E. Volovik, Topological Lifshitz transitions, Low Temp. Phys. **43**, 47 (2017).

[30] H. F. Yang, L. X. Yang, Z. K. Liu, Y. Sun, C. Chen, H. Peng, M. Schmidt, D. Prabhakaran, B. A. Bernevig, C. Felser, B. H. Yan, and Y. L. Chen, Topological Lifshitz transitions and Fermi arc manipulation in Weyl semimetal NbAs, Nat. Commun. **10**, 3478 (2019).

[31] S. A. Ekahana, Y. W. Li, Y. Sun, H. Namiki, H. F. Yang, J. Jiang, L. X. Yang, W. J. Shi, C. F. Zhang, D. Pei, C. Chen, T. Sasagawa, C. Felser, B. H. Yan, Z. K. Liu, and Y. L. Chen, Topological Lifshitz transition of the intersurface Fermi-arc loop in $NbIrTe_4$, Phys. Rev. B **102**, 085126 (2020).

[32] D. Kumar, C.-H. Hsu, R. Sharma, T.-R. Chang, P. Yu, J. Wang, G. Eda, G. Liang, and H. Yang, Room-temperature nonlinear Hall effect and wireless radiofrequency rectification in Weyl semimetal $TaIrTe_4$, Nat. Nanotechnol. **16**, 421 (2021).

[33] K. Koepernik, D. Kasinathan, D. V. Efremov, S. Khim, S. Borisenko, B. Büchner, and J. van den Brink, $TaIrTe_4$: A ternary type-II Weyl semimetal, Phys. Rev. B **93**, 201101(R) (2016).

[34] L. Li, H.-H. Xie, J.-S. Zhao, X.-X. Liu, J.-B. Deng, and X.-R. Hu, Ternary Weyl semimetal $NbIrTe_4$ proposed from first-principles calculation, Phys. Rev. B **96**, 024106 (2017).

[35] I. Belopolski, P. Yu, D. S. Sanchez, Y. Ishida, T. R. Chang, S. S. Zhang, S. Y. Xu, H. Zheng, G. Chang, G. Bian, H. T. Jeng, T. Kondo, H. Lin, Z. Liu, S. Shin, and M. Z. Hasan, Signatures of

a time-reversal symmetric Weyl semimetal with only four Weyl points, Nat. Commun. **8**, 942 (2017).

[36] X. Zhou, Q. Liu, Q. Wu, T. Nummy, H. Li, J. Griffith, S. Parham, J. Waugh, E. Emmanouilidou, B. Shen, O. V. Yazyev, N. Ni, and D. Dessau, Coexistence of tunable Weyl points and topological nodal lines in ternary transition-metal telluride $TaIrTe_4$, Phys. Rev. B **97**, 241102(R) (2018).

[37] G. Kresse and J. Hafner, Ab initio molecular dynamics for open-shell transition metals, Phys. Rev. B **48**, 13115 (1993).

[38] J. P. Perdew, K. Burke, and M. Ernzerhof, Generalized Gradient Approximation Made Simple, Phys. Rev. Lett. **77**, 3865 (1996).

[39] H. Inoue, A. Gyenis, Z. Wang, J. Li, S. W. Oh, S. Jiang, N. Ni, B. A. Bernevig, and A. Yazdani, Quasiparticle interference of the Fermi arcs and surface-bulk connectivity of a Weyl semimetal, Science **351**, 1184 (2016).

[40] H. Zheng, G. Bian, G. Chang, H. Lu, S. Y. Xu, G. Wang, T. R. Chang, S. Zhang, I. Belopolski, N. Alidoust, D. S. Sanchez, F. Song, H. T. Jeng, N. Yao, A. Bansil, S. Jia, H. Lin, and M. Zahid Hasan, Atomic-Scale Visualization of Quasiparticle Interference on a Type-II Weyl Semimetal Surface, Phys. Rev. Lett. **117**, 266804 (2016).

[41] P. Deng, Z. Xu, K. Deng, K. Zhang, Y. Wu, H. Zhang, S. Zhou, and X. Chen, Revealing Fermi arcs and Weyl nodes in $MoTe_2$ by quasiparticle interference mapping, Phys. Rev. B **95**, 245110 (2017).

[42] C. L. Lin, R. Arafune, R. Y. Liu, M. Yoshimura, B. Feng, K. Kawahara, Z. Ni, E. Minamitani, S. Watanabe, Y. Shi, M. Kawai, T. C. Chiang, I. Matsuda, and N. Takagi, Visualizing type-II Weyl points in tungsten ditelluride by quasiparticle interference, ACS Nano **11**, 11459 (2017).

[43] D. Iaia, G. Chang, T.-R. Chang, J. Hu, Z. Mao, H. Lin, S. Yan, and V. Madhavan, Searching for topological Fermi arcs via quasiparticle interference on a type-II Weyl semimetal $MoTe_2$, npj Quantum Mater. **3**, 38 (2018).

[44] N. Morali, R. Batabyal, P. K. Nag, E. Liu, Q. Xu, Y. Sun, B. Yan, C. Felser, N. Avraham, and H. Beidenkopf, Fermi-arc diversity on surface terminations of the magnetic Weyl semimetal Co_3Sn_2S, Science **365**, 1286 (2019).

[45] Z. Wang, J. Olivares, H. Namiki, V. Pareek, K. Dani, T. Sasagawa, V. Madhavan, and Y. Okada, Visualizing superconductivity in a doped Weyl semimetal with broken inversion symmetry, Phys. Rev. B **104**, 115102 (2021).

[46] See Supplemental Material at http://link.aps.org/supplemental/10.1103/PhysRevB.105.075110 for more details of STM/S measurements and DFT calculations, which also includes Refs. [34,52–56].

[47] C. Thomsen, J. Strait, Z. Vardeny, H. J. Maris, J. Tauc, and J. J. Hauser, Coherent Phonon Generation and Detection by Picosecond Light Pulses, Phys. Rev. Lett. **53**, 989 (1984).

[48] B. He, C. Zhang, W. Zhu, Y. Li, S. Liu, X. Zhu, X. Wu, X. Wang, H.-h. Wen, and M. Xiao, Coherent optical phonon oscillation and possible electronic softening in WTe_2 crystals, Sci. Rep. **6**, 30487 (2016).

[49] M. V. Gustafsson, T. Aref, A. F. Kockum, M. K. Ekström, G. Johansson, and P. Delsing, Propagating phonons coupled to an artificial atom, Science **346**, 207 (2014).

[50] A. Nakamura, T. Shimojima, Y. Chiashi, M. Kamitani, H. Sakai, S. Ishiwata, H. Li, and K. Ishizaka, Nanoscale imaging of unusual photoacoustic waves in thin flake VTe_2, Nano Lett. **20**, 4932 (2020).

[51] X. Jia, S. Zhang, R. Sankar, F. C. Chou, W. Wang, K. Kempa, E. W. Plummer, J. Zhang, X. Zhu, and J. Guo, Anomalous Acoustic Plasmon Mode from Topologically Protected States, Phys. Rev. Lett. **119**, 136805 (2017).

[52] C. Franchini, R. Kováčik, M. Marsman, S. S. Murthy, J. He, C. Ederer, and G. Kresse, Maximally localized Wannier functions in $LaMnO_3$ within PBE + U, hybrid functionals and partially self-consistent GW: An efficient route to construct ab initio tight-binding parameters for e_g perovskites, J. Phys.: Condens. Matter **24**, 235602 (2012).

[53] G. W. Bryant, Surface states of ternary semiconductor alloys: Effect of alloy fluctuations in one-dimensional models with realistic atoms, Phys. Rev. B **31**, 5166 (1985).

[54] P. Roushan, J. Seo, C. V. Parker, Y. S. Hor, D. Hsieh, D. Qian, A. Richardella, M. Z. Hasan, R. J. Cava, and A. Yazdani, Topological surface states protected from backscattering by chiral spin texture, Nature (London) **460**, 1106 (2009).

[55] M. P. Lopez Sancho, J. M. Lopez Sancho, J. M. L. Sancho, and J. Rubio, Highly convergent schemes for the calculation of bulk and surface Green functions, J. Phys. F **15**, 851 (1985).

[56] A. Togo and I. Tanaka, First principles phonon calculations in materials science, Scr. Mater. **108**, 1 (2015).